Journal of Oceanography, Vol. 66, pp. 553 to 569, 2010

Uncertainties in Global Mapping of Argo Drift Data at the Parking Level

KATSURO KATSUMATA[1]* and HIROSHI YOSHINARI[2]

[1]*Research Institute for Global Change, JAMSTEC, Natsushima, Yokosuka 237-0061, Japan*
[2]*Hokkaido National Fisheries Research Institute, Fisheries Research Agency, Katsurakoi, Kushiro 085-0802, Japan*

(Received 9 September 2009; in revised form 7 April 2010; accepted 4 June 2010)

We used Argo float drift data to estimate average ocean currents at 1000 dbar depth from early 2000 to early 2010. Our estimates cover the global oceans, except for marginal seas and ice-covered regions, at a resolution of 1 degree in latitude and longitude. The estimated flow field satisfies the horizontal boundary condition of no flow through the topography, and is in geostrophic balance. We also estimated the uncertainty in the average flow field, which had a typical magnitude of 0.03 ms^{-1}. The uncertainty is relatively large (>0.03 ms^{-1} in both the zonal and meridional directions) near the Equator and in the Southern Ocean. The array bias, which is the bias due to the horizontal gradient in the spatial density of the float data, is generally negligible, with an average magnitude outside the equatorial region of 0.007 ms^{-1}, becoming relatively large (>0.01 ms^{-1}) only near the coastal regions. The measurement uncertainty is assumed to be spatially uniform and includes errors due to the Argos positioning system, internal clock drift, unknown surface drift before submerging or after surfacing, and unknown drifts during ascent and descent between the surface and the parking depth. We found that the overall uncertainty was not sensitive to the assumed value of the measurement uncertainty $(\varepsilon_m)^{1/2}$ when $(\varepsilon_m)^{1/2} < 0.01$ ms^{-1} but it increased with $(\varepsilon_m)^{1/2}$ for $(\varepsilon_m)^{1/2} > 0.01$ ms^{-1}.

Keywords:
· Argo floats,
· absolute velocity,
· objective mapping,
· geostrophy.

1. Introduction

Argo floats revolutionised observational oceanography with their quantity of the hydrographic data they collected. In addition to hydrographic data, Argo floats provide data for estimating current velocities at the parking level through the positions at the surface fixed by satellites. The velocity information provides a solution to the long-standing problem in physical oceanography of estimating the unknown integration constant of the thermal wind relationship.

Lebedev *et al*. (2007) compiled the Argo satellite fixes to provide a raw data set of the velocities both at the parking level and at the surface. Argo floats are designed to repeat a cycle of descending from the surface to a parking level, drifting following a preset pressure or density, ascending to the surface while measuring hydrographic data such as salinity and temperature, and then transmitting data through the satellite system, primarily the System Argos satellites, while at the surface. The approach used by Lebedev *et al*. (2007) to estimate the drift at the parking level is the simplest one, where the velocity is given by the distance divided by the time between the last position fix before descending and the first position fix after ascending.

Using a subset of the Lebedev *et al*. (2007) data from the parking level, we have estimated the quasi-global mean flow field at 1000 dbar over the period from 2000 to 2010. In this paper, we investigate various uncertainties in the mapping process. The extreme variability in the ocean means that heavy smoothing both in time and space is required. We followed the method described by Davis (1998, 2005), who derived the mean flow using the drift data from the ALACE floats (Davis *et al*., 1992), the predecessor of the Argo floats. The strengths of this method are that it is statistically optimal (it is objective mapping using the Gauss-Markov theorem), that the flow is in geostrophic balance, and that the flow satisfies the horizontal boundary condition of no normal flow at the horizontal boundaries.

* Corresponding author. E-mail: k.katsumata@jamstec.go.jp

The resultant global map of the flow has many potential applications, such as estimating absolute velocities from hydrography, constraining box inverse models (e.g., Wijffels *et al*., 2001), and evaluating the performance of numerical models. The product is publicly available online from the JAMSTEC's Argo website (http://www.jamstec.go.jp/ARGO/argo_web/G-YoMaHa/index_e.html).

2. Types of Uncertainty in Drift Data Mapping

This study focuses on the uncertainties in the global mapping of drift data. In this section, we review the uncertainties involved in estimating the mean flow field using Argo floats.

2.1 Array bias

The array bias is the bias resulting from the horizontal gradient in the spatial density of float data. Davis (1991) discussed fundamental issues in characterising lateral mean oceanic transport using current-following floats. The key quantity is the eddy diffusivity κ estimated from single particle statistics,

$$\kappa_{jk}(\boldsymbol{x},t) = -\left\langle v_j'\left(t_0|\boldsymbol{x},t_0\right) r_k'\left(t_0 - t|\boldsymbol{x},t_0\right)\right\rangle, \tag{1}$$

where the subscripts i, j, k denote the spatial coordinates in the east, north, and vertical directions, respectively, the angle brackets are Eulerian ensemble (or time) averaging, $v(t|\boldsymbol{x}, t_0)$ is the Lagrangian velocity at time t of a particle that passes through position $\boldsymbol{x}$ at time t_0 with the prime symbol denoting departure from the Lagrangian mean and, similarly, $r(t|\boldsymbol{x}, t_0)$ is the position at time t of a particle that passes through position $\boldsymbol{x}$ at time t_0. The diffusivities for other components (e.g., κ_{ii}, κ_{ij} ...) can be defined in the same manner. The diffusivity κ is a function of time, but generally oceanic flows are so turbulent that after some time lag T_0, the velocity mean product $\langle v_j'(t_0|\boldsymbol{x}, t_0) v_k'(t_0 - t|\boldsymbol{x}, t_0)\rangle$ vanishes. Then for time intervals longer than T_0,

$$\kappa_{jk}(\boldsymbol{x},t) \to \kappa_{jk}^{\infty}(\boldsymbol{x}). \tag{2}$$

When estimating the Eulerian mean velocity U in a region A, the velocities sampled in A are averaged over a time interval much longer than T_0, during which the mean particle density is approximately steady. The estimate is known to be biased (equation (2.17) of Davis (1991));

$$\tilde{u} = \frac{\int_A \mathrm{d}\boldsymbol{x}\left[U(\boldsymbol{x})C(\boldsymbol{x}) - \kappa^{\infty}(\boldsymbol{x})\cdot\nabla C(\boldsymbol{x})\right]}{\int_A \mathrm{d}\boldsymbol{x} C(\boldsymbol{x})}, \tag{3}$$

where $\tilde{u}$ is the estimated average velocity, $U(\boldsymbol{x})$ is the true mean, and $C(\boldsymbol{x})$ is the ensemble-space average of the particle density, i.e.,

$$C(\boldsymbol{x}) = \left\langle \sum_n \delta\left[\boldsymbol{x} - \boldsymbol{r}\left(t|n\right)\right]\right\rangle, \tag{4}$$

where δ is the Dirac delta function, and n is a shorthand for the labelling coordinates $(\boldsymbol{x}, t_0)$.

The second term of the right-hand side of Eq. (3) is the array bias. The array bias can be corrected using estimated diffusivity κ^{∞} and float density $C(\boldsymbol{x})$. The diffusivity estimates are also subject to an array bias, but the magnitude is difficult to estimate (Davis, 1991). We have neglected the array bias in our diffusivity estimates.

2.2 Measurement uncertainties

Davis (1991) also discussed potential uncertainties such as molecular effects, bias and dispersion caused by internal waves, and low-frequency vertical motion. He found that all of these are negligible when estimating large-scale mean flows. These uncertainties apply to isobaric floats in general, but the following uncertainties are known to apply specifically to Argo floats. First, *positioning error by the Argos satellite system* is generally less than 1000 m (Ichikawa *et al*., 2001), which amounts to about 1×10^{-3} ms^{-1} for velocity estimation over 10 days. Second, *clock drift* exists for the internal clock in some floats. Park *et al*. (2005) found a systematic drift rate of about 370 s year^{-1} in four floats deployed in the Sea of Japan, which is negligible when calculating the averaged velocity over 10 days, but the clock time can suddenly jump which could cause substantial error in the resultant velocity estimate. Third, *unknown surface drift before submerging and after surfacing* can be a significant source of error because surface flows are generally much stronger than the deeper flows and several hours can elapse before the satellite communication starts after surfacing (Ichikawa *et al*., 2001). Last, *unknown drifts during ascent and descent between the surface and the parking depth* can also potentially cause significant errors. Assuming a linear shear between the surface and the parking depth, Lebedev *et al*. (2007) estimated the mean magnitude of this error to be 53×10^{-3} ms^{-1}, which is likely to be an overestimate, because the vertical profile of the horizontal flow is more surface intensified than linearly sheared. Park *et al*. (2005) estimated that this error is less than, or at most comparable, to the surface drift error. A similar conclusion was reached by Ichikawa *et al*. (2001), who estimated the surface drift error at 0 to 12×10^{-3} ms^{-1} and the ascending/descending drift error at 1 to 13×10^{-3} ms^{-1} for four Argo floats.

Some of these errors could be corrected using the meta data from the floats (Park *et al*., 2005). A project is underway to produce a better Argo drift data set using the meta data (ANDRO—Argo New Displacements, Rannou Ollitrault, Ollitrault and Rannou (2009)). For this study, however, we take a different approach; although the measurement uncertainty is different for each drift datum, we use a representative value, ε_m, for all drift data and examine the sensitivity of the overall uncertainty on ε_m. We use $(\varepsilon_m)^{1/2} = 5 \times 10^{-3}$ ms^{-1} unless otherwise noted.

2.3 Sampling uncertainties

In this section, we summarise the method by Davis (1991) to estimate the sampling uncertainties. The reader is referred to the original paper (Section 4, in particular) for detail.

Oceanic flows are so turbulent that the largest contribution to the overall uncertainties is expected to come from turbulent eddies. When [i] the velocity statistics and float distribution are homogeneous over the averaging area and stationary over the averaging time, [ii] the sample size is large, and [iii] Corrsin's conjecture applies, Davis (1991) shows that the sampling uncertainty in the mean velocity estimate is given by

$$\left(\delta U_k\right)^2 = \int_L \mathrm{d}t \int_L \mathrm{d}t' \int_A \mathrm{d}\boldsymbol{x} \int_A \mathrm{d}\boldsymbol{x}' \Big[E_{kk}\left(\boldsymbol{x}-\boldsymbol{x}', t-t'\right) \cdot \sum_n \sum_m \left\langle \delta\left[\boldsymbol{x}-\boldsymbol{r}\left(t|n\right)\right] \delta\left[\boldsymbol{x}'-\boldsymbol{r}\left(t|m\right)\right] \right\rangle \Big] \Big/ N^2 L^2 , \quad (5)$$

where $E_{jk}(x, t)$ is the time- and space-lagged covariance of the j and k components of $\boldsymbol{u}'$, A is the sampling area, L is the sampling period, and N is the average number of samples over L.

Corrsin's conjecture (Shlien and Corrsin, 1974) states that a particle's position and its velocity are statistically independent. When computing a statistics such as (5) from Lagrangian data, one needs to deal with an ensemble averaging of, say, $\delta(\boldsymbol{x} - \boldsymbol{r}(t|n))u_k' \times \delta(\boldsymbol{x} - \boldsymbol{r}(t|m))\, u_l'$. Using Corrsin's conjecture, it is possible to proceed by separating the averaging as $\langle \delta(\boldsymbol{x} - \boldsymbol{r}(t|n))\delta(\boldsymbol{x} - \boldsymbol{r}(t|m))\rangle \langle u_k' u_l' \rangle$. The applicability of the conjecture to turbulence in general is not proven (e.g., Ott and Mann, 2005), but the conjecture appears accurate in oceanic turbulence (Davis, 1983).

With a further assumption of long averaging time, large averaging area, and statistically independence of particle position, (5) is simplified to

$$\left(\delta U_k\right)^2 = 2\frac{\kappa_{kk}^{\infty}}{NL}\left(1 + \frac{N-1}{N}\frac{\lambda_k^2}{A}\right), \quad (6)$$

where λ_k is the integral length scale and κ_{kk}^{∞} was defined in (2).

The estimate given by Eq. (6) suggests that the sampling covariance of the drift data is inversely proportional to the sampling period L. Thus, the statistically optimal averaging is

$$\tilde{\boldsymbol{u}} = \frac{1}{T}\sum_{n=1}^{N}\left[\boldsymbol{x}\left(t_n + \tau_n|n\right) - \boldsymbol{x}\left(t_n|n\right)\right], \quad (7)$$

where τ_n is the interval between two position fixes and

$$T = \sum_{n=1}^{N} \tau_n . \quad (8)$$

The position of $\tilde{\boldsymbol{u}}$ is assigned to the midpoint of $\boldsymbol{x}(t_n + \tau_n|n)$ and $\boldsymbol{x}(t_n|n)$. Similarly, the uncertainty due to geostrophic depth correction, explained later in Subsection 3.2, is weighted by τ_n^2 when averaging.

The sampling uncertainty in the diffusivity estimate has also been discussed by Davis (1991). In addition to the three assumptions listed above (homogeneous and stationary statistics, large sample size, and applicability of Corrsin's conjecture), it is necessary to assume the joint-normal distribution of v' and r', stationary Lagrangian covariance, and a long observation period to reach an evaluation

$$\lim_{t\to\infty} \frac{\left(\delta\kappa(t)\right)^2}{\left(\kappa^{\infty}\right)^2} \propto \frac{t}{N} . \quad (9)$$

This approximation (9) holds for large t, but the Argo floats need to ascend to the surface for communication, every 10 days in most cases. This interruption in drift at depth makes it difficult to obtain reliable records for periods longer than 10 days. The integral timescale T_0 was measured in several studies in the North Atlantic using SOFAR floats, which do not need to surface and also have better time resolutions. The results are summarised in table 1 of Böning (1988). For the zonal direction, T_0 varied from 4.8 to 18 days (simple mean 12.5 days) and for the meridional direction from 4.6 to 10.1 days (simple mean 7.6 days) at various depths from 700 to 2200 m. A similar correlation timescale was reported by Lavender *et al*. (2005). Therefore we expect that (9) is marginally applicable with the Argo sampling period of 10 days. Assuming T_0 = 10 days and defining $\kappa^{\infty} = \kappa(t = T_0)$, we discarded data with sampling periods shorter than 9 days. If the sampling periods were different from T_0 = 10 days, we used (9) to "normalise" the diffusivity error $\delta\kappa$ at $t = T_0$.

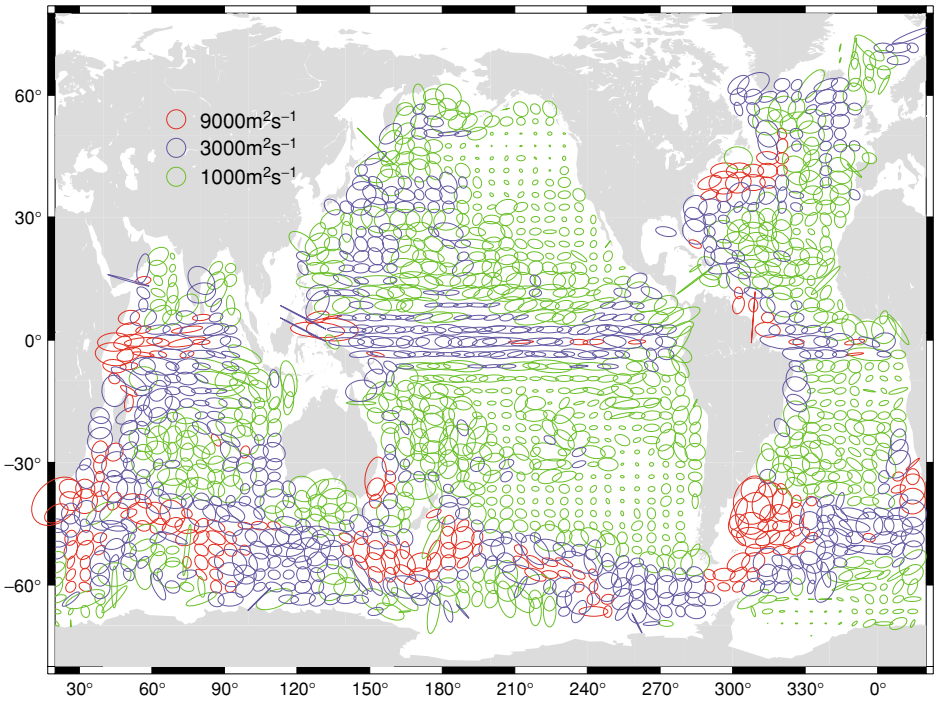

Fig. 1. Diffusivity as estimated by the area-averaging method. Ellipse axes are the principal axes of the horizontal diffusivity according to the colour coding. Strong diffusivity is found in the strong currents. Near the Equator the zonal diffusivity is stronger than the meridional diffusivity.

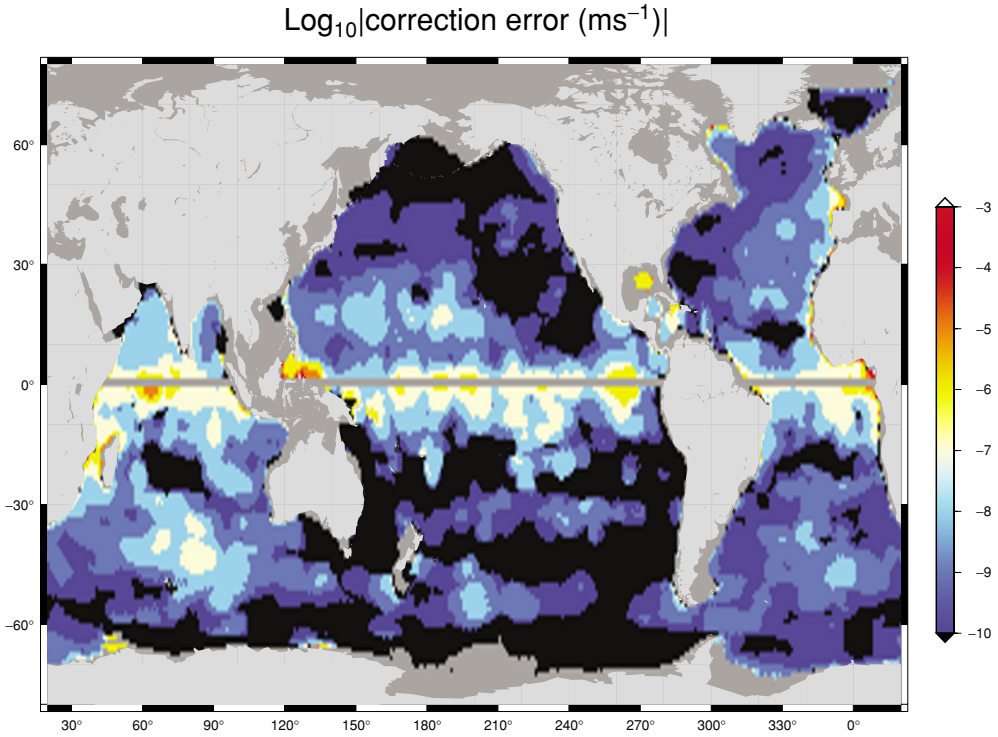

Fig. 2. Magnitude of the uncertainties in the geostrophic depth correction (ms^{-1}) calculated by perturbing the temperature and salinity during the geostrophic depth correction by one standard deviation as estimated in the original climatology data (Gouretski and Koltermann, 2004). Colours indicate the magnitude of the correction uncertainty in log scale.

In practice, we evaluated Eq. (1) to estimate the diffusivity from each drift datum when area-averaging was used (Fig. 1). Uncertainty in the diffusivity was estimated assuming each datum as independent, making a correction for the sampling period with (9). The estimated diffusivity gives an estimate of the mean velocity variance through

$$\left\langle u'^2_{jk} \right\rangle = 2\frac{\kappa^{\infty}_{jk}}{T_0}. \tag{10}$$

Note that (5) or (6) means that (10) does not translate into the expected covariance of the mean velocity $\boldsymbol{U}(\boldsymbol{x})$ unless it is divided by the appropriate degrees of freedom of the data set. Referring to (5), the degrees of freedom in the data sample is defined as

$$N^* = N^2L^2 \times \left(\int_L \mathrm{d}t \int_L \mathrm{d}t' \int_A \mathrm{d}\boldsymbol{x} \int_A \mathrm{d}\boldsymbol{x}' \left[e_{kk}(\boldsymbol{x}-\boldsymbol{x}', t-t') \cdot \sum_n \sum_m \left\langle \delta\left[\boldsymbol{x}-\boldsymbol{r}(t|n)\right] \delta\left[\boldsymbol{x}-\boldsymbol{r}(t|m)\right] \right\rangle \right] \right)^{-1}, \tag{11}$$

where e_{kk} is the covariance function. We assumed a Gaussian function

$$e_{kk}(\boldsymbol{x}-\boldsymbol{x}', t-t') = \exp\left\{ -|\boldsymbol{x}-\boldsymbol{x}'|^2 / D_0^2 - (t-t')^2 / T_0^2 \right\}. \tag{12}$$

Table 1 of Böning (1988) shows the length scales of 25 to 82 km (zonal) and 13 to 54 km (meridional). Noting that these data were taken at mid-latitudes and that the length scales vary with the Coriolis parameter, we selected a length scale of D_0 = 100 km. As stated above, T_0 = 10.0 days. The sampling uncertainty was thus evaluated as

$$\varepsilon_e = 2\frac{\kappa^{\infty}_{kk}}{T_0 N^*}. \tag{13}$$

3. Method

3.1 Quality control

The Argo drift data, YoMaHa'07, is available online (http://apdrc.soest.hawaii.edu/projects/yomaha). Monthly and near-realtime updates are also available therein. The discussion in this paper is based upon the monthly updated version of March 2010. The original data set (as of June 2007) consists of about 270,000 drift velocities, the basic statics of which are provided in Lebedev *et al.* (2007). The March 2010 version now has about 570,000 drift velocities. We took several steps to ensure the quality of data used in our analysis. First, the data from floats with the cycle lengths shorter than 9 days were discarded, because the short cycle length contaminates the diffusivity estimates (see Eq. (9)). Second, the drift data that included possible groundings were removed. Drift data were assumed to indicate grounding if both of the two following conditions were met: [i] the parking depth recorded in the YoMaHa'07 data are within 20% of the bottom depth from the ETOPO5 data set*, and [ii] the drift speed was less than 50% of the float average drift speed. Here float average drift speed is the average of the drift speed collected by a single float over repeated cycles. Third, the drift velocities more than five standard deviations (calculated for the velocities collected by a single float) away from the float average drift speed were removed as outliers. Approximately 4.9% and 0.05% of data were removed as suspected groundings and outliers, respectively.

3.2 Depth correction

As shown by Lebedev *et al.* (2007), the parking depths of the floats varied from 400 dbar to 2000 dbar. After the quality control checks described in Subsection 3.1, 66% of the floats in the data set had a parking depth of 1000 dbar, which was used as our target depth. Data from depths other than 1000 dbar were corrected by adding a geostrophic shear calculated from the WOCE Global Hydrographic Climatology (Gouretski and Koltermann, 2004). The climatology data come with error estimates for temperature (ΔT) and salinity (ΔS). The uncertainties involved in the depth correction, ε_c, were evaluated by repeating the shear calculation with $T \pm \Delta T$ and $S \pm \Delta S$.

The magnitude of the uncertainty due to geostrophic depth correction (Fig. 2) was generally negligible ($<10^{-5}$ ms^{-1}) and concentrated in the equatorial regions.

3.3 Seasonal variation in the equatorial regions

As demonstrated by Davis (1998), the flows in the equatorial region (latitude < 5°) are dominated by low-frequency zonal variability (Fig. 3), which must be filtered out to accurately determine the mean field.

As in the study by Davis (2005), reanalysis data from a numerical ocean general circulation model were used. The model is an updated version of the ocean reanalysis model described by Masuda *et al.* (2003, 2009). The model is based on the GFDL MOM version 3 with a horizontal grid resolution of 1° resolution and 46 vertical levels,

*Data Announcement 88-MGG-02, Digital relief of the Surface of the Earth. NOAA, National Geophysical Data Center, Boulder, Colorado, 1988 (http://www.ngdc.noaa.gov/mgg/global/etopo5.HTML).

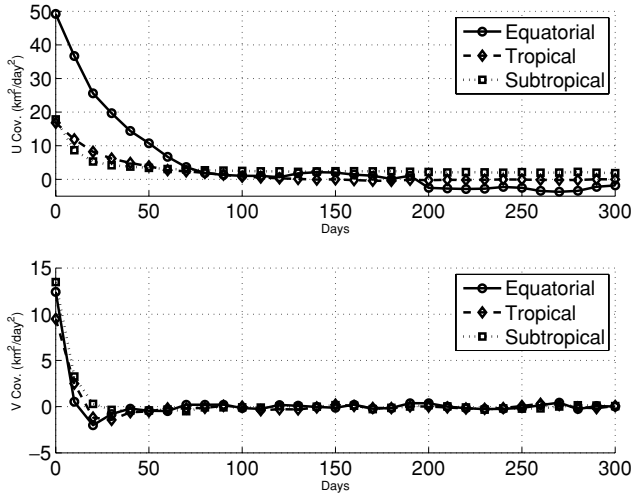

Fig. 3. Time-lagged covariances for zonal (upper panel) and meridional (lower panel) components of drift velocities following a single float. Subtropical (latitude > 15°) and tropical (15° > latitude > 5°) velocities are isotropic and decorrelation timescales are a few tens of days. Equatorial (latitude < 5°) velocities are dominated by zonal components and have a zonal flow timescale of over 50 days.

forced by the National Centers for Environmental Prediction/National Center for Atmospheric Research (NCEP/NCAR) atmospheric reanalysis data. The model output was constrained in the least-squares sense to the observed data using the four-dimensional variational assimilation method. The set of observed data was the EN3 quality controlled data (Ingleby and Huddleston, 2007) plus recent data from JAMSTEC hydrography cruises (e.g., Uchida and Fukasawa, 2005).

The spatial patterns were extracted by the empirical orthogonal functions (EOF) of the model output at 1038 m depth. The EOFs were calculated separately for the Pacific, Indian, and Atlantic oceans (but shown on one map; Fig. 4).

The spatial functions were then fitted to the depth-corrected Argo drift velocities averaged over 3 months using the least-squares fit. Four spatial modes were used in each basin. The four modes explained 31, 17, 6, 5%, respectively, of the variance in the model Pacific Ocean. The corresponding contributions in the Indian Ocean were 24, 19, 14, 10%, and 28, 21, 5, 5 in the Atlantic Ocean. As the quantity of the data increased after 2003, the fit worked reasonably well, except in the Indian Ocean where the semi-annual variation was overestimated in the model (Fig. 5). As part of this process, the data from years before 2000 were discarded; this helped to fulfil the assumption of constant spatial density of float coverage discussed in relation to Eq. (3).

Although the model output fits the observations reasonably well (Fig. 5), it cannot completely remove the equatorial zonal velocity covariance (Fig. 6). With this remaining covariance and the vanishing Coriolis parameter, the mean velocity estimates in the equatorial regions are accompanied by large errors in the resultant map, calling for extra care when interpreting the data.

3.4 Area averaging and local function fit

The objective mapping requires prior estimates of the covariances, which we estimated from the area-averaged mean field. Following Davis (2005), the averaging area takes into consideration the steering effect of the bathymetry by defining the distance between points A and B as

$$r^2 = r_{AB}^2 + \mu^2 \left(\log \frac{\min(H_A, H_B)}{\max(H_A, H_B)} \right)^2, \qquad (14)$$

where r_{AB} is the geographical distance between A and B, and H_i is the depth at $i = A, B$. The averaging area is a "circle" with $r < R$, where R is defined such that its area is equal to $\pi(300\ \mathrm{km})^2$. In the actual calculation, the circle is approximated by a dodecagon. Following Davis (2005), the constant μ is set at 300 km The topography data are ETOPO5 smoothed with a 100 km Gaussian filter.

The area-averaged mean velocity at 1000 dbar (Fig. 7) shows the major ocean currents. There are no data for the shallow marginal seas (the Sea of Okhotsk, the Mediterranean, and the Indonesian Seas) or ice covered polar regions.

Simple area averaging fails to distinguish temporal and spatial variabilities. The two can be separated by fitting spatial functions locally. Following Davis (2005), we used five nondivergent functions at (x, y) within the averaging circle around the grid point (x_0, y_0)

$$\begin{aligned} \boldsymbol{U}(x,y) = {} & a_1\hat{\boldsymbol{x}} + a_2\hat{\boldsymbol{y}} + a_3\hat{\boldsymbol{x}}(y - y_0) + a_4\hat{\boldsymbol{y}}(x - x_0) \\ & + a_5\left[\hat{\boldsymbol{x}}(x - x_0) - \hat{\boldsymbol{y}}(y - y_0)\right], \end{aligned} \qquad (15)$$

where $\hat{\boldsymbol{x}}$ and $\hat{\boldsymbol{y}}$ are eastward and northward unit vectors, respectively. All data within the "circle" with R = 300 km and μ = 300 km were used to estimate the amplitudes $a_1, a_2, \ldots, a_5$. We used the statistically optimal estimation (Gauss-Markov theorem) by minimising

$$J = \left(\boldsymbol{d}_f - F_f\boldsymbol{a}_f\right)^T E_f^{-1}\left(\boldsymbol{d}_f - F_f\boldsymbol{a}_f\right) + \boldsymbol{a}_f^T B^{-1}\boldsymbol{a}_f, \qquad (16)$$

where the trajectory velocities within the "circle" is

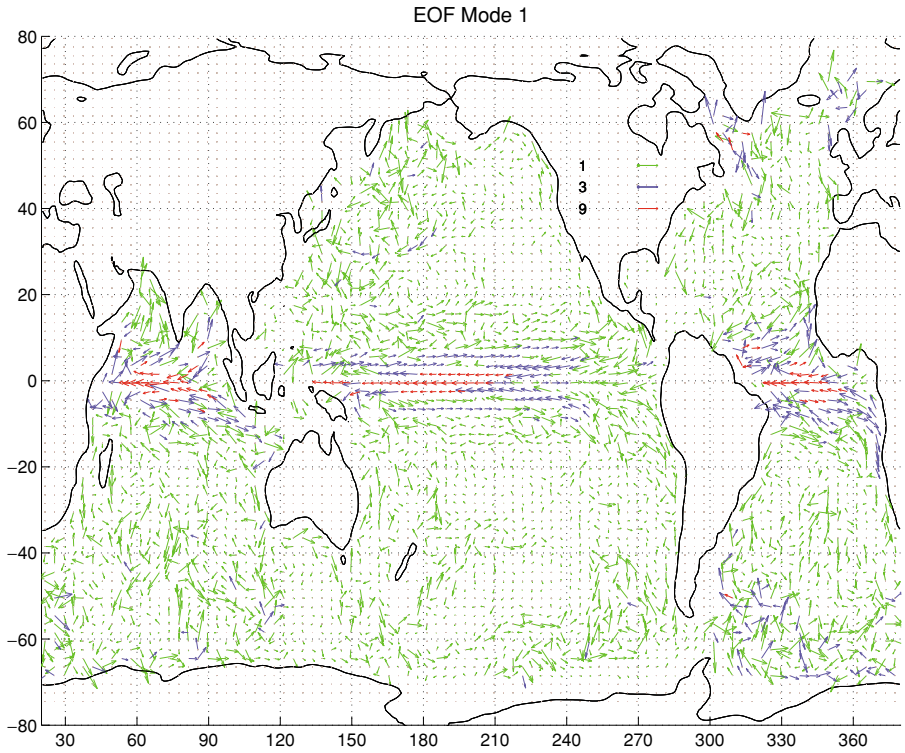

Fig. 4. The first mode of the empirical orthogonal function (EOF) of the monthly output from a numerical model from 1987 to 2006. The EOFs were calculated separately for the Pacific, Indian, and Atlantic oceans, and plotted together on a single map. The amplitude is arbitrary.

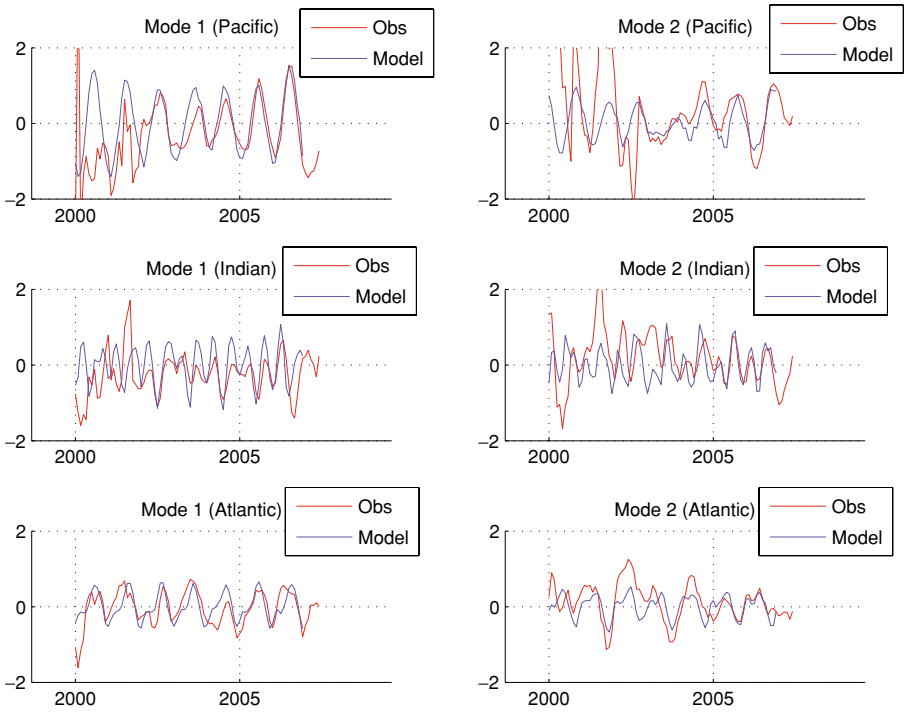

Fig. 5. Time series of the spatial empirical orthogonal functions. The first two modes are shown for the Pacific, Indian, and Atlantic oceans.

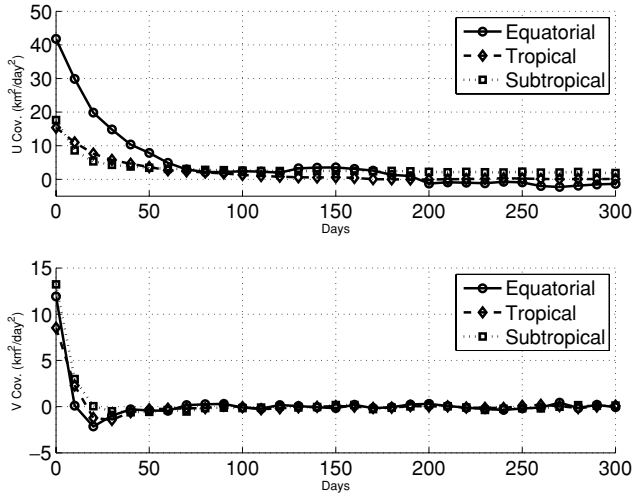

Fig. 6. Same as in Fig. 3, but after subtracting out seasonal variations estimated by the numerical model.

$\boldsymbol{d}_f$, $\boldsymbol{a}_f = (a_1, a_2, a_3, a_4, a_5)^T$, F_f is the matrix representing (15). The noise covariance E_f has the same diagonal components

$$\varepsilon = \varepsilon_e + \varepsilon_c + \varepsilon_m, \tag{17}$$

where ε_e is the sampling error (Eq. (13)), due to eddies, ε_c is the error due to geostrophic depth correction (Subsection 3.2) and ε_m is the measurement error (Subsection 2.2). We used the value of $\varepsilon_m = (5 \times 10^{-3}\ \mathrm{ms}^{-1})^2$ unless otherwise noted. The signal covariance A_f is diagonal; $B_{11} = B_{22} = (10^{-2}\ \mathrm{ms}^{-1})^2$, $B_{33} = B_{44} = (10^{-4}\ \mathrm{ms}^{-1})^2$, $B_{55} = (5 \times 10^{-5}\ \mathrm{ms}^{-1})^2$, with the distances $x - x_0$ and $y - y_0$ normalised by the "radius" R = 300 km.

The resultant flow field (Fig. 8) appears very similar to the area-averaged case (Fig. 7), but the difference (not shown) shows that the function fit mean velocity tends to estimate the slightly weaker Antarctic Circumpolar Current.

3.5 Objective mapping

3.5.1 Basis functions

Given covariances that decrease with distance and time (e.g., Fig. 3), observed data are often mapped to a grid using a spatially and/or temporally localised covariance function (e.g., Gaussian). On the other hand, Davis (2005) used a different approach, where the mapped field is spanned by a set of basis functions. The advantage of this approach is that the basis functions satisfy the horizontal boundary condition of no flow through the topography, such that the mapped field satisfies the same boundary condition.

Two types of the spatial functions were prepared (Fig. 9); interior modes, and landmass modes. The interior mode (n, m) is the solution of the Poisson equation

$$\nabla^2 \phi(\boldsymbol{r}, n, m) = \exp\left(i\boldsymbol{k}(n,m) \cdot \boldsymbol{r}\right), \tag{18}$$

with the boundary condition

$$\phi = 0$$

on land. The landmass modes are the solution of (18) with the right-hand side replaced with 0 and the boundary condition $\phi = 1$ on one particular landmass and $\phi = 0$ on all other landmasses. Unlike the analysis of Davis (2005), our analysis is global so that no open ocean modes are required.

The wavenumber vector in (18) is given by

$$\boldsymbol{k}(n,m) = \left(n\pi / N_x, m\pi / N_y\right), \tag{19}$$

where N_x = 360, N_y = 165, indicating the number of grids in the zonal and meridional directions, respectively. The mapping region is from 180°W to 180°E in longitude and from 84.5°S to 79.5°N in latitude. In this work, we used the wavenumbers from (n, m) = (1, 1) to (n, m) = (48, 48). The expected covariance of the interior modes is given as Gaussian in the wavenumber space

$$\exp\left[-\left(\boldsymbol{k}(n,m) \cdot \boldsymbol{L}^2\right)^2 \Big/ 2\right], \tag{20}$$

where we chose $\boldsymbol{L}$ = (4.0, 1.375).

Using the ETOPO5 topography data smoothed by a 100 km Gaussian filter, we took the 700 m isobath to define the horizontal boundaries. Under these conditions, eight landmasses are found. The expected or *a prior* amplitude of the landmass modes can be prescribed by independent estimates of the transport between the landmasses. Here we used the geostrophic transport estimated using WOCE Global Hydrographic Climatology (Gouretski and Koltermann, 2004) and past observations in major straits and channels between the landmasses. These estimates are summarised in Table 1. The Ekman transport is assumed to have oscillatory seasonal variability with zero long-term average, which does not affect the transports in Table 1.

The covariances of the interior and landmass modes were all diagonal since we expected no relationships between different modes.

3.5.2 Objective mapping

The mathematical expression of the objective mapping is to find a vector $\boldsymbol{a}$ that minimises the cost function

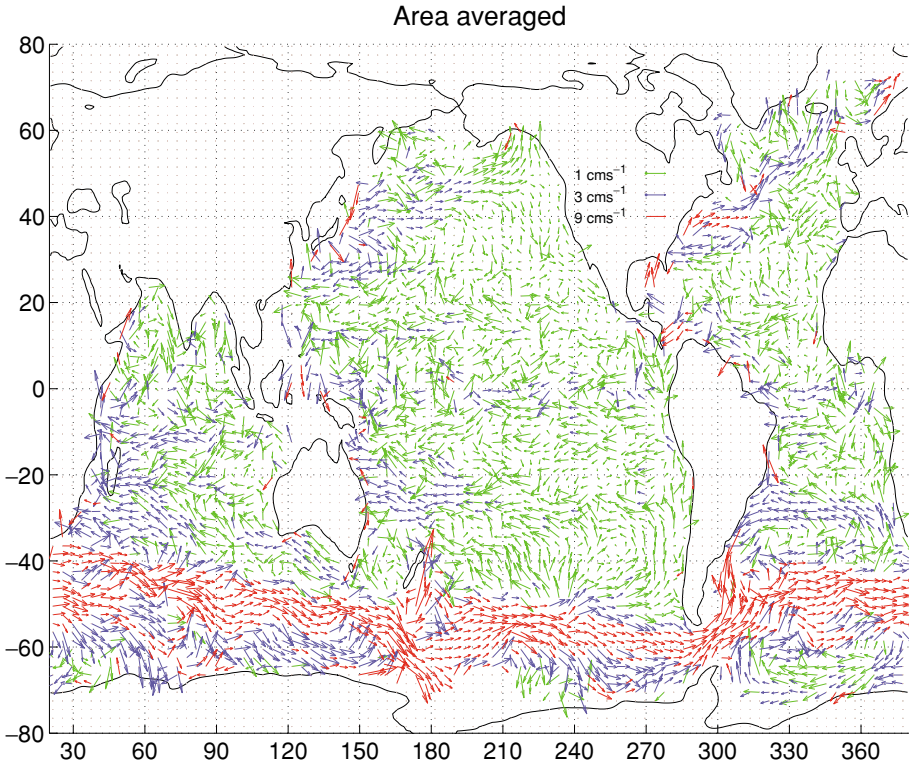

Fig. 7. Area-averaged mean velocity vectors at 1000 dbar.

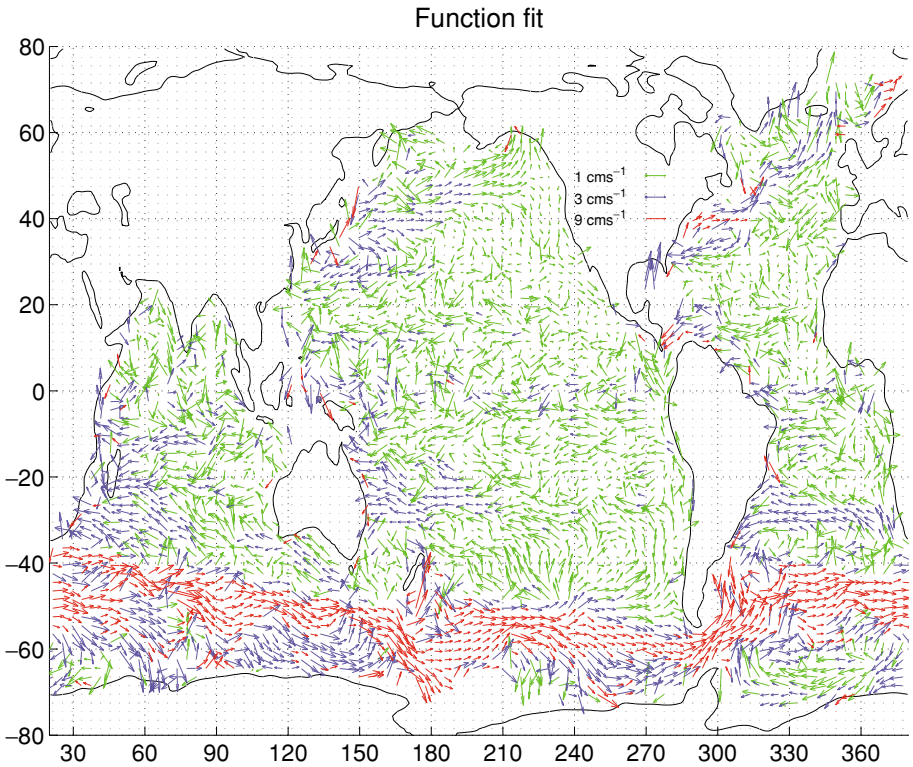

Fig. 8. Function-fit mean velocity vectors at 1000 dbar.

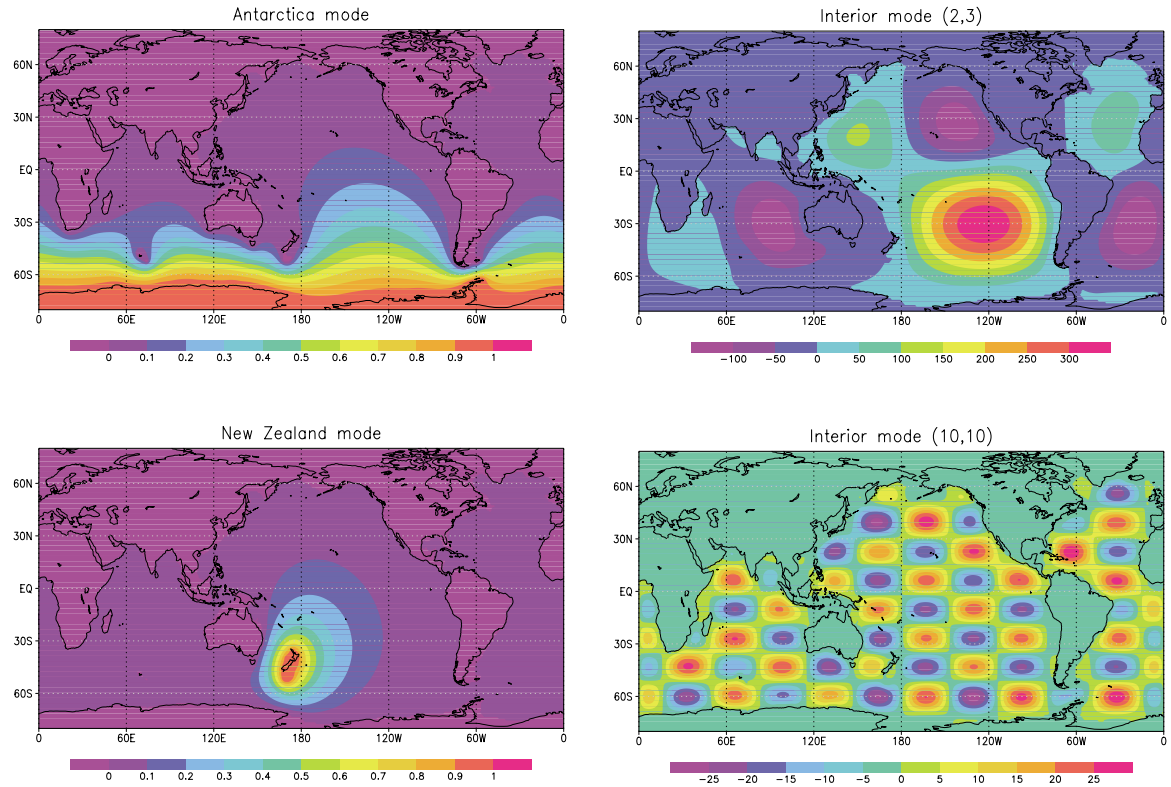

Fig. 9. Examples of basis functions, showing the landmass modes for the Antarctica (left top) and New Zealand (left bottom), and the interior modes with the wavenumbers (2,3) (right top) and (10, 10) (right bottom).

Table 1. Landmass modes for basis functions including expected (*a priori*) amplitude (A) based on the observed (Obs.) transports between landmasses.

Landmass	A ($\times 10^3$ m^{2}s^{-1})	Obs. (Sv), location	Reference
Asia–America–Europe	0	—	
Antarctica	71.4	134, Drake Passage	Nowlin and Klinck (1986)
Madagascar	4.5	8.6, Mozambique Channel	Harlander *et al.* (2008)
Kerguelen North	63.6	14.0, between Kerguelen and Antarctica	McCartney and Donohue (2007)
Kerguelen South	63.6	14.0, between Kerguelen and Antarctica	McCartney and Donohue (2007)
Australia–PNG	5.9	13.5, Indonesian Throughflow	Gordon *et al.* (2008)
Philippines	1.5	2.4, Luzon Strait	Qu *et al.* (2004)
New Zealand	9.6	10.1, between Australian and NZ	Ridgway *et al.* (2008)

$$J = (\boldsymbol{d} - HF\boldsymbol{a})^T E^{-1}(\boldsymbol{d} - HF\boldsymbol{a}) + \boldsymbol{a}^T A^{-1}\boldsymbol{a}, \qquad (21)$$

where $\boldsymbol{d}$ is the velocities estimated by the floats, F consists of the column vectors of the basis functions explained in the previous section, and $\boldsymbol{a}$ is the amplitude of the basis functions. According to the Gauss-Markov theorem, the minimum uncertainty is achieved by taking E as the noise covariance matrix and A as the expected covariance of $\boldsymbol{a}$. The data $\boldsymbol{d}$ and the noise covariances E are taken from the results of the function fit (Subsection 3.4).

The data $\boldsymbol{d}$ and the estimated parameters $\boldsymbol{a}$ do not have to be the same quantity, which makes it possible to determine a scalar field $F\boldsymbol{a}$ instead of the velocity. The matrix H converts the scalar field $F\boldsymbol{a}$ into the velocity. Following Davis (2005), we employed the geostrophic pressure p as the scalar field. The advantage of this choice is that the estimated velocity field satisfies the geostrophic balance

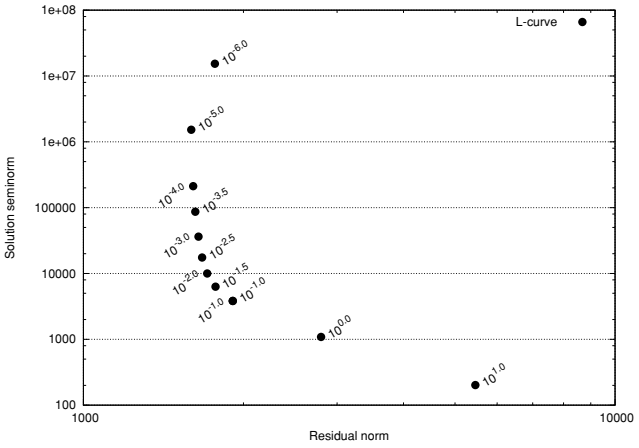

Fig. 10. *L*-curve. The abscissa is the residual norm (the first term in Eq. (21)) and the ordinate is the solution seminorm (the second term in Eq. (21)). The numbers beside the solid circles indicate λ. When λ is small, the minimisation of (21) with regard to $\boldsymbol{a}$ "overfits" the solution so that the magnitude of the solution becomes large. When λ is large, the minimisation is achieved by "oversimplifying" $\boldsymbol{a}$ and the solution does not explain the data well. The best balance is achieved near the corner of the *L*-curve.

$$-fv = -\frac{1}{\rho_0}\frac{\partial p}{\partial x},$$

$$-fv = -\frac{1}{\rho_0}\frac{\partial p}{\partial x}, \tag{22}$$

where f is the Coriolis parameter and ρ_0 is a typical density of sea water. The matrix H is, then, a discretised expression of (22). To avoid singularity, the Coriolis parameter f at the Equator (where $f = 0$) was replaced by that at latitude 0.1°. From 0.5°S to 0.5°N, no depth correction was performed and those data collected from depths other than 1000 dbar in this latitude band were discarded.

Although the covariances of the landmass modes are estimated from the data listed in Table 1, we note here that for the interior modes, only the magnitude of the covariances *relative to each other* can be fixed by (20). We therefore used a control parameter λ to optimise the overall covariance (cov) A such that

diag$A$ = [cov of landmass modes λ(cov of interior modes)].

We used the *L*-curve method proposed by Hansen (1992) to find the best value for λ. In this method, the behaviour of the cost function (21) is characterised by plotting the solution semi-norm (the second term in (21)) against the residual norm (the first term in (21)). The plot resembles the letter "*L*" and the corner point gives the best λ, where the balance between the two terms is reached. Figure 10 shows the *L*-curve. The corner point is somewhere between $\lambda = 10^{-1}$ and $\lambda = 10^{-2}$.

Once the parameter λ was fixed, the minimisation of (21) was achieved following the SVD method described in subsection 2.5 of Wunsch (2006).

4. Results and Discussion

4.1 Objectively mapped mean velocity

We chose a value for λ of 10^{-2} (Fig. 10) but the results were not much different for $\lambda = 10^{-1.5}$. The objectively-mapped velocity field is much smoother than the function-fit version (compare Figs. 11 and 8). Near the horizontal boundaries, in particular, the flow tends to be smoother in the objectively-mapped field because of the basis functions that satisfy the horizontal boundary conditions (Fig. 9).

Some blank regions in the function-fit map (e.g., south of 65°S) are now filled, but the lack of in situ data is evident in the relatively high uncertainties in map of geostrophic pressure (Fig. 12).

Although we have calculated the geostrophic pressure across the Equator, the dynamics near the Equator are fundamentally different from those at mid-latitudes (e.g., chapter 11 of Gill, 1982) and the assumption of the geostrophy (22) or non-divergence breaks down in this region. We therefore regard the geostrophic pressure near the Equator as erroneous. This region is removed by deleting the data with error speed larger than 0.08 ms^{-1}. This criterion also removes data from the marginal seas with little floats (the Indonesian Seas, the Sea of Okhotsk, the Gulf of Mexico, and the Ross Sea).

The behaviour of the uncertainty associated with the velocity is easier to see when the uncertainty in the geostrophic pressure (Fig. 12(b)) is converted into the uncertainty in the velocity (Fig. 13). By using the geostrophy (22), the uncertainties in the velocities (δu, δv) are evaluated as

$$\left(\delta v_i\right)^2 \le \frac{2}{\rho_0^2 f^2}\frac{q_{i-1}+q_{i+1}}{\left(2\Delta x\right)^2},$$

$$\left(\delta u_j\right)^2 \le \frac{2}{\rho_0^2 f^2}\frac{q_{i-1}+q_{i+1}}{\left(2\Delta y\right)^2}, \tag{23}$$

where (i, j) are indices for zonal and meridional grids, respectively, Δx and Δy are grid sizes (=1°), and q is the squared uncertainty in the geostrophic pressure at the grid estimated by the objective mapping. Since the interior modes with the finest resolution has the zonal and me-

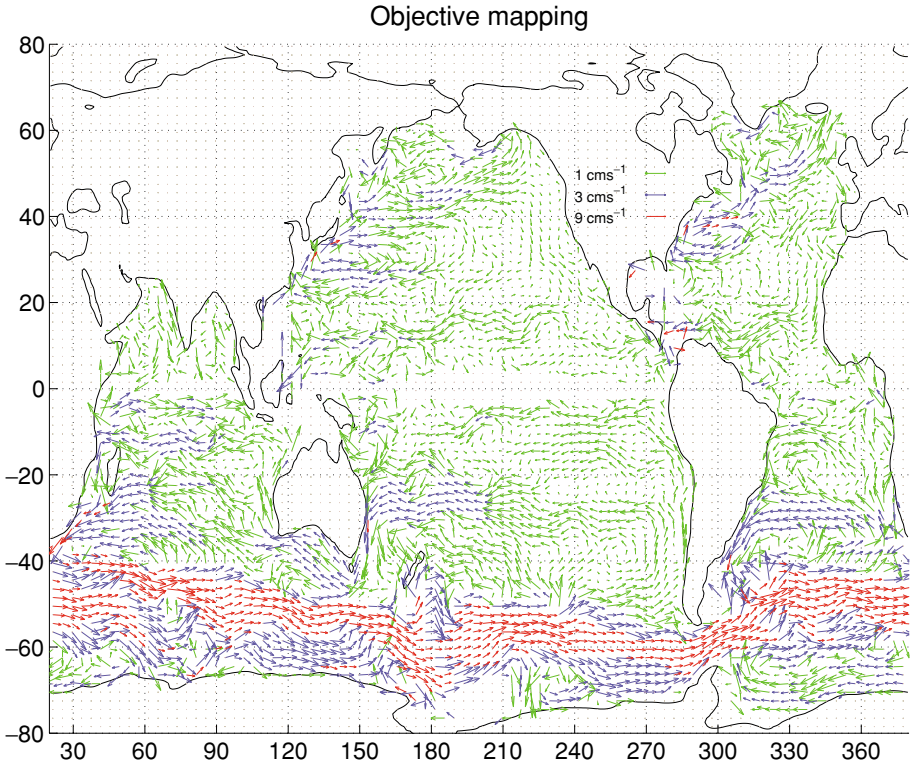

Fig. 11. Objectively-mapped mean velocity vectors at 1000 dbar.

ridional wavenumbers of 48 (see the discussion following Eq. (19)), the uncertainties in neighbouring grids are likely to be correlated. If two quantities a, b with covariances $\langle(\delta a)^2\rangle$, $\langle(\delta b)^2\rangle$, respectively, are correlated, the covariance in the sum $c = a + b$ is evaluated as

$$\begin{aligned}&\left\langle (a+\delta a+b+\delta b)^2 \right\rangle \\ &= \left\langle (a+b)^2 \right\rangle + \left\langle (\delta a)^2 + (\delta b)^2 \right\rangle + 2\langle \delta a \delta b \rangle, \end{aligned} \tag{24}$$

where the covariances δa, δb are not correlated with a, b. With

$$\delta a \delta b \le \frac{(\delta a)^2 + (\delta b)^2}{2},$$

the covariance in $c = a + b$ can be evaluated as

$$\left\langle (\delta c)^2 \right\rangle \le 2\left\langle (\delta a)^2 + (\delta b)^2 \right\rangle. \tag{25}$$

The coefficient 2 on the right-hand side of (23) is thus fixed. The uncertainty is relatively large in data-sparse regions towards the coast and in the Southern Ocean. The bands of relatively high error (>0.03 ms^{-1}) extend from Africa to the Weddel Sea and from Australia to the Ross Sea. These are the regions with high variability (Fig. 1) but with a low data density, which suggests the sampling uncertainty due to active eddies is the main source of the uncertainty. The error is much lower in the Pacific and Atlantic oceans away from the Equator, where the float density is relatively high and the eddy activity is relatively low.

Davis (2005) estimated the geostrophic pressure field in the South Pacific and South Indian oceans using the trajectories from about 530 ALACE floats deployed between 1991 and 1996. His results (figures 16 and 17 in Davis, 2005) appear very similar to our results (Fig. 12). A close look reveals the following differences: [i] the eastward extent of the South Pacific subtropical gyre as shown by the 10 cm contour shrank; [ii] the meridional location of the Antarctic Circumpolar Current shifted slightly southward; and [iii] the peak of the South Indian subtropical gyre becomes weaker. Interestingly, the first and second points are consistent with recent reports of the changes in the hydrographic status in the Southern Ocean, namely, the spin-up of the South Pacific subtropical gyre (Roemmich *et al.*, 2007) and the poleward mi-

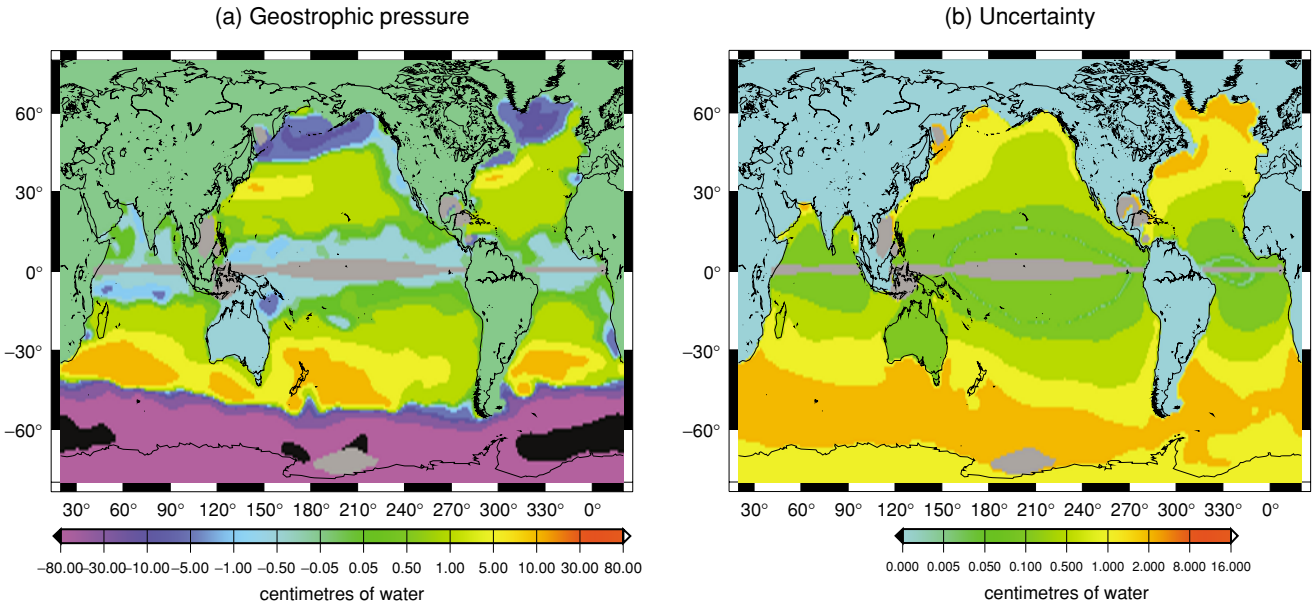

Fig. 12. Objectively-mapped (a) geostrophic pressure and (b) uncertainty in geostrophic pressure at 1000 dbar. The pressure has been divided by $\rho_0 \times g$ so that it has the dimension of length (cm). Figure 11 was produced by the spatial derivative of (a) using (22).

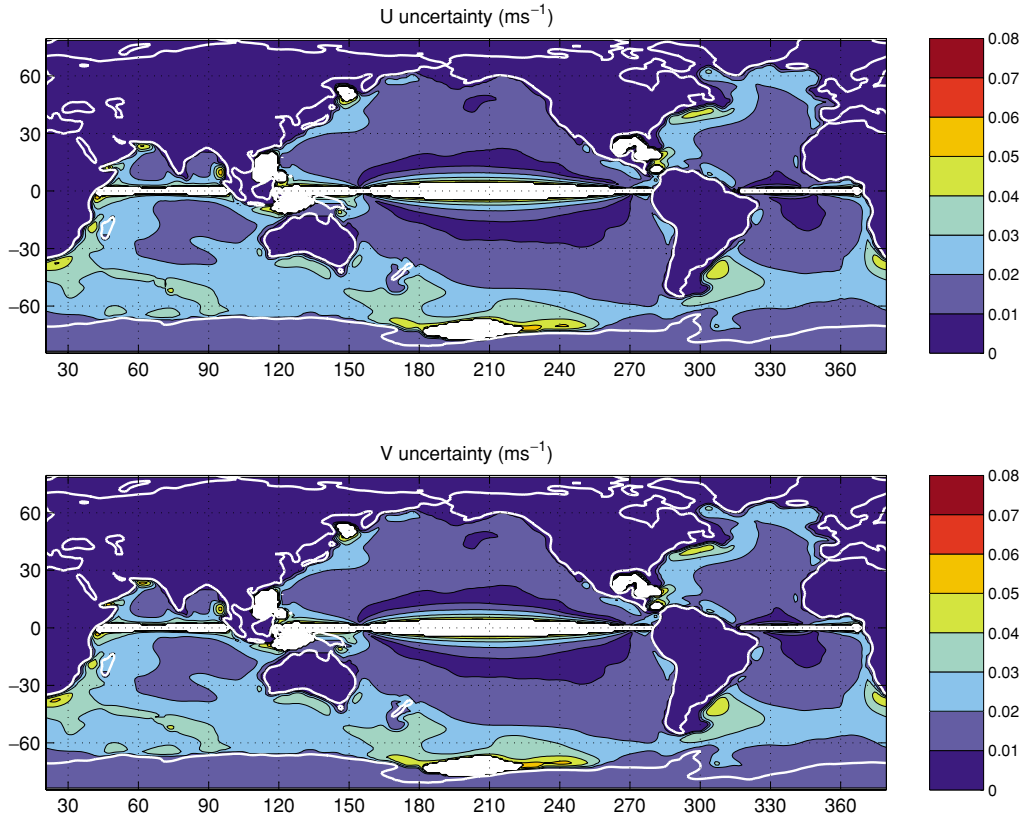

Fig. 13. Upper bounds of the estimated uncertainty in the zonal and meridional velocities.

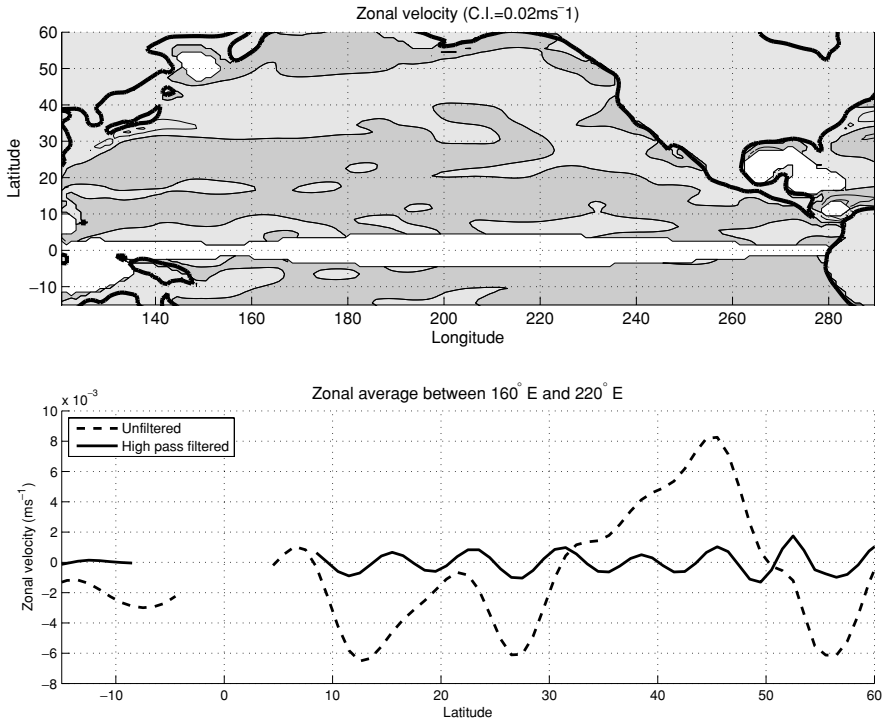

Fig. 14. Zonal velocities. The upper panel shows the zonal velocity with the shading indicating westward velocity. The contour interval is 0.02 ms^{-1}. The lower panel is a meridional section of the zonally-averaged zonal velocity between 160°E and 140°W. The broken line shows the zonal velocity; features include the eastward flowing Kuroshio Extension around 45°N, the westward flowing North Equatorial Current with the core at 13°N, the eastward flowing Equatorial Countercurrent around 5°N and the westward flowing South Equatorial Current around 10°S. The solid line shows the high-pass-filtered profile with a cutoff wavelength of 10° of latitude using the fourth-order Butterworth filter.

gration of the Antarctic Circumpolar Current (Gille, 2008). Owing to the paucity of data, particularly in the 1990s, however, the differences in the geostrophic pressure estimated from the float trajectories are not statistically significant and further work is necessary to confirm the third point listed above. As the trajectory data accumulate, it might be possible in the future to detect long-term changes in the circulation using the float trajectories only.

4.2 Zonal jets and southern supergyre

Before discussing array bias and the measurement error, we note two interesting features of the estimated mean velocity: zonally alternating jets and the Southern Hemisphere supergyre.

Zonally alternating jets in mid- and deep oceans have been a focus of recent researches (e.g., Nakano and Hasumi, 2005; Maximenko *et al*., 2005) and it is possible that these jets are observable in the Argo drift velocities. We prepared a map showing the distribution of the zonal velocity in the Pacific at 1000 dbar (Fig. 14, upper panel), comparable to figure 4 of Nakano and Hasumi (2005). On this map, the zonally alternating jets are not obvious. We then prepared a meridional section of the zonally-averaged zonal velocities (Fig. 14, lower panel). The distribution of zonal velocities contains a fluctuating component, which is emphasised by a high-pass filter. This zonally alternating component has a meridional wavelength of approximately 8° of latitude (Fig. 14, lower panel). This is roughly twice the wavelength reported by Nakano and Hasumi (2005) or Maximenko *et al*. (2005). We suspect that our results show a low-pass-filtered zonal jet structure because the mapping process filters out the high-wavenumber components. Note that the radius of the area averaging (Fig. 7) is $R \approx 300$ km, which is coincidentally a typical meridional length scale reported for this feature by Nakano and Hasumi (2005), Maximenko *et al*. (2005).

Ridgway and Dunn (2007) used hydrographic data to describe the Southern Hemisphere supergyre, a nested system of subtropical gyres, that connects the subtropical South Pacific and South Indian gyres. Our results, based on an independent data set, also show the existence of such a gyre (Fig. 15). One difference from the hydrographic analysis (Ridgway and Dunn, 2007; Roemmich, 2007) is that our results show the gyre extending into the Atlantic Ocean, although there is high

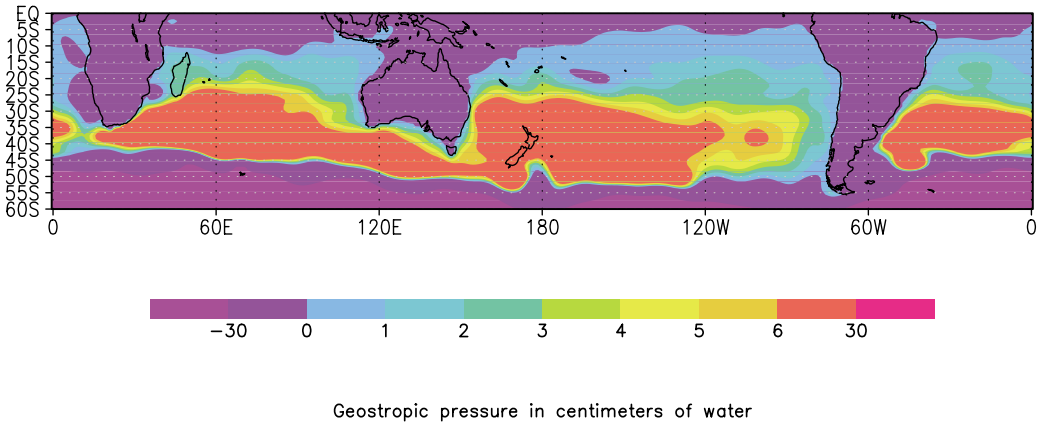

Fig. 15. Geostrophic pressure field in the Southern Hemisphere using a different contouring scheme than in Fig. 12. The 2 cm and 3 cm contours are evident not only in the Pacific and Indian oceans, but also in the Atlantic Ocean.

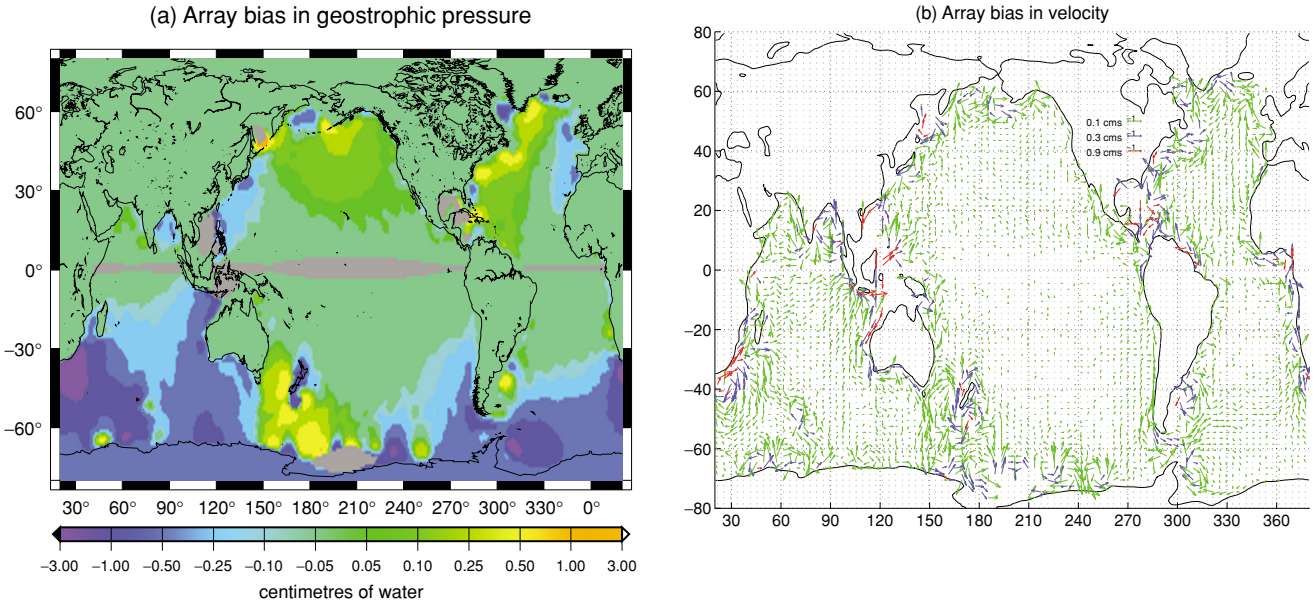

Fig. 16. Array bias expressed in (a) pressure and (b) velocity. Array bias was estimated by subtracting the map with array bias correction from the map without array bias correction. As seen in Eq. (3), the array bias is large where the gradient in the data density is large.

uncertainty in the region south of Africa (Fig. 13) and we cannot conclusively determine whether the Atlantic and Indian gyres are connected or not. The variability in this region is known to be high with occasional ring detachments from the energetic Agulhas Current (Lutjeharms, 2006). It is also possible that an average description of this region, such as ours, is dependent on the averaging period.

4.3 Array bias

Figure 16 shows the distribution of the array bias. The definition of the bias (the rightmost term in (3)) means that it is large in areas with a large spatial gradient in the data density and a large diffusivity. These conditions are met near the boundaries and in the Southern Ocean. The mean magnitude of the array bias, except for in the equatorial region (within latitude ±5°) is 0.7×10^{-3} ms^{-1}, but near the coast, the magnitude reaches 15×10^{-3} ms^{-1}.

4.4 Measurement uncertainties

The objective mapping yields estimated uncertainty ((2.342) of Wunsch, 2006) of the mapping along with the

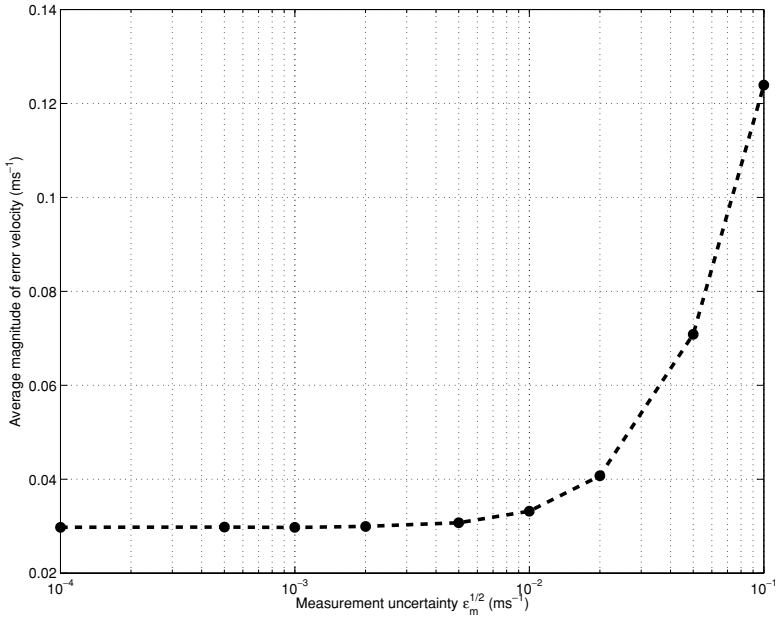

Fig. 17. Sensitivity of the overall uncertainty to the assumed uniform measurement error. When the measurement error is less than 10^{-2} ms^{-1}, the overall uncertainty, as measured by the average of the magnitude of the error velocity, is not sensitive to the measurement error. However, the overall error increases with the increasing measurement error above 10^{-2} ms^{-1}.

mapped field. We call this uncertainty as the overall uncertainty and we examine the sensitivity of the overall uncertainty to the measurement error ε_m (Fig. 17) by repeating the objective mapping with different ε_m's. The overall uncertainty is not sensitive to the measurement error when the measurement error is less than 10^{-2} ms^{-1}. This means that efforts to improve the measurement error will not yield improved results unless the measurement error is larger than 10^{-2} ms^{-1}. On the other hand, if the measurement error is likely to be larger than 10^{-2} ms^{-1}, a reduced measurement error will contribute to reducing the overall error. Ideally, the measurement error should be estimated for each drift datum along with the surfacing and submerging time stamps, the Argos system error, and information on shear and surface currents, but not all Argo drift data come with such useful information, and efforts for reliable estimation of the measurement error and its correction should continue.

We note that the overall uncertainty shown in Fig. 17 applies specifically to the current study parameters: a global analysis with a horizontal resolution of 1° and data from more than 9 years. A different mapping technique or the size of sample (e.g., regional studies, studies focusing on particular times or seasons) would probably yield a different dependency of the overall uncertainty on the measurement errors.

5. Summary

We estimated average flows at 1000 dbar from the drift data of Argo floats from early 2000 to 2010 on a quasi-global, 1° grid. The estimated flows are statistically optimal, are in geostrophic balance, and satisfy the condition of no flow through the horizontal boundaries. The uncertainties in the resultant flows originate from the sampling variability, the measurement uncertainties, and the array bias. The uncertainties are large near the Equator and along the coast of Antarctica coasts, and are not sensitive to the measurement uncertainties if the measurement uncertainties are less than about 10^{-2} ms^{-1}. The array bias is negligible except in coastal regions.

The sampling and measurement uncertainties will decrease as more drift data are accumulated. An increase in data also should yield a more accurate estimate of the eddy diffusivity leading to a better estimate of the array bias in coastal regions.

Acknowledgements

The Argo data were collected and made freely available by the International Argo Project and associated contributing national programs (http://www.argo.ucsd.edu, http://argo.jcommops.org). Argo is a pilot program of the Global Ocean Observing System.

References

Böning, C. W. (1988): Characteristics of particle dispersion in the North Atlantic: an alternative interpretation of SOFAR float results. *Deep-Sea Res.*, **35**, 1379–1385.

Davis, R. E. (1983): Oceanic property transport, Lagrangian

particle statistics, and their prediction. *J. Mar. Res.*, **41**, 163–194.
Davis, R. E. (1991): Observing the general circulation with floats. *Deep-Sea Res.*, **38**, Suppl. 1, S531–S571.
Davis, R. E. (1998): Preliminary results from directly measuring middepth circulation in the tropical and South Pacific. *J. Geophys. Res.*, **103**, 24619–24639.
Davis, R. E. (2005): Intermediate-depth circulation of the Indian and South Pacific Oceans measured by autonomous floats. *J. Phys. Oceanogr.*, **35**, 683–707.
Davis, R. E., D. C. Webb, L. A. Regier and J. Dufour (1992): The Autonomous Lagrangian Circulation Explorer (ALACE). *J. Atmos. Oceanic Technol.*, **9**, 264–285.
Gill, A. E. (1982): *Atmosphere-Ocean Dynamics*. Academic Press, California, 622 pp.
Gille, S. T. (2008): Decadal-scale temperature trends in the Southern Hemisphere Ocean. *J. Climate*, **21**, 4749–4765.
Gordon, A., D. Susanto, S. Wijffels, J. Sprintall, R. Molcard, H. Van Aken, A. Ffield, A. Supangat and I. Jaya (2008): Introduction/overview of INSTANT Indonesian Throughflow 2004–2006 as observed by INSTANT. Ocean Sciences Meeting, American Geophysical Union.
Gouretski, V. V. and K. P. Koltermann (2004): WOCE Global Hydrographic Climatology. Bundesamtes für Seeschifffahrt und Hydrographie, Report 35.
Hansen, P. C. (1992): Analysis of discrete ill-posed problems by means of the L-curve. *SIAM Rev.*, **34**, 561–580.
Harlander, U., H. Ridderinkhof, M. W. Schouten and W. P. M. de Ruijter (2009): Long-term observations of transport, eddies, and Rossby waves in the Mozambique Channel. *J. Geophys. Res.*, **114**, C02003, doi:10.1029/2008JC004846.
Ichikawa, Y., Y. Takatsuki, K. Mizuno, N. Shikama and K. Takeuchi (2001): Estimation of drifting velocity and error at parking depth for Argo float. *JAMSTECR*, **44**, 81–89.
Ingleby, B. and M. Huddleston (2007): Quality control of ocean temperature and salinity profiles—historical and real-time data. *J. Mar. Syst.*, **65**, 158–175.
Lavender, K. L., W. B. Owens and R. E. Davis (2005): The mid-depth circulation of the subpolar North Atlantic Ocean as measured by subsurface floats. *Deep-Sea Res. I*, **52**, 767–785.
Lebedev, K. V., H. Yoshinari, N. A. Maximenko and P. W. Hacker (2007): YoMaHa'07: Velocity data assessed from trajectories of Argo floats at parking level and at the sea surface. *IPRC Technical Note*, **4**(2). Available online at http://apdrc.soest.hawaii.edu/projects/yomaha/index.html
Lutjeharms, J. R. E. (2006): *The Agulhas Current*. Springer, Berlin, 329 pp.
Masuda, S., T. Awaji, N. Sugiura, Y. Ishikawa, K. Baba, K. Horiuchi and N. Komori (2003): Improved estimates of the dynamical state of the North Pacific Ocean from a 4 dimensional variational data assimilation. *Geophys. Res. Lett.*, **30**, 1868, doi:10.1029/2003GL017604.
Masuda, S., T. Awaji, T. Toyoda, Y. Shikama and Y. Ishikawa (2009): Temporal evolution of the equatorial thermocline associated with the 1991–2006 ENSO. *J. Geophys. Res.*, **114**, C03015, doi:10.1029/2008JC004953.
Maximenko, N. A., B. Bang and H. Sasaki (2005): Observational evidence of alternating zonal jets in the world ocean. *Geophys. Res. Lett.*, **32**, L12607, doi:10.1029/2005GL02272.
McCartney, M. S. and K. A. Donohue (2007): A deep cyclonic gyre in the Australian-Antarctic Basin. *Prog. Oceanogr.*, **75**, 675–750.
Nakano, H. and H. Hasumi (2005): A series of zonal jets embedded in the broad zonal flows in the Pacific obtained in eddy-permitting ocean general circulation models. *J. Phys. Oceanogr.*, **35**, 474–488.
Nowlin, W. D., Jr. and J. M. Klinck (1986): The physics of the Antarctic Circumpolar Current. *Rev. Geophys.*, **24**, 469–491.
Ollitrault, M. and J.-P. Rannou (2009): The mean-depth circulation of the Atlantic with Argo float displacements from the ANDRO Atlas (AOML and Coriolis Data only). *Argo Science Workshop 3*, Hangzhou, China.
Ott, S. and J. Mann (2005): An experimental test of Corrsin's conjecture and some related ideas. *New J. Phys.*, **7**, 142, doi:10.1088/1367-2630/7/1/142.
Park, J. J., K. Kim, B. A. King and S. C. Riser (2005): An advanced method to estimate deep currents from profiling floats. *J. Atmos. Oceanic Technol.*, **22**, 1294–1304.
Qu, T., Y. Y. Kim, M. Yaremchuk, T. Tozuka, A. Ishida and T. Yamagata (2004): Can Luzon Strait Transport play a role in conveying the impact of ENSO to the South China Sea? *J. Climate*, **17**, 3644–3657.
Ridgway, K. R. and J. R. Dunn (2007): Observational evidence for a Southern Hemisphere oceanic supergyre. *Geophys. Res. Lett.*, **34**, L13612, doi:10.1029/2007GL03039.
Ridgway, K. R., R. C. Coleman, R. J. Bailey and P. Sutton (2008): Decadal variability of East Australian Current transport inferred from repeated high-density XBT transects, a CTD survey and satellite altimetry. *J. Geophys. Res.*, **113**, C08039, doi:10.1029/2007JC004664.
Roemmich, D. (2007): Super spin in the southern seas. *Nature*, **449**, 34–35.
Roemmich, D., J. Gilson, R. Davis, P. Sutton, S. Wijffels and S. Riser (2007): Decadal spinup of the Southern Pacific subtropical gyre. *J. Phys. Oceanogr.*, **26**, 162–173.
Shlien, D. J. and S. Corrsin (1974): A measurement of Lagrangian velocity autocorrelation in approximately isotropic turbulence. *J. Fluid Mech.*, **62**, 255–271.
Uchida, H. and M. Fukasawa (2005): WHP P6, A10, I3/I4 Revisit data book, vol. 2. JAMSTEC, Yokosuka, Japan, 129 pp. Available online at http://whpo.ucsd.edu
Wijffels, S. E., J. M., Toole and R. Davis (2001): Revisiting the South Pacific subtropical circulation: A synthesis of World Ocean Circulation Experiment observations along 32°S. *J. Geophys. Res.*, **106**, 19481–19513.
Wunsch, C. (2006): *Discrete Inverse and State Estimation Problems with Geophysical Fluid Applications*. Cambridge University Press, Cambridge, 371 pp.